CONF-9103165--4

ELECTRON SCATTERING FROM TENSOR-POLARIZED DEUTERONS IN THE VEPP-3 ELECTRON STORAGE RING

ANL/CP--73761

DE91 017299

David H. Potterveld

Argonne National Lab.
9700 S. Cass Ave.
Argonne, Il. 60439

ELASTIC SCATTERING

Within the plane wave impulse approximation, the differential cross section for unpolarized elastic electron-deuteron scattering may be written in the familiar Rosenbluth form:

$$\frac{d\sigma}{d\Omega} = \sigma_m \Big[A(Q^2) + B(Q^2) \tan^2(\theta/2) \Big] \equiv \sigma_0 \qquad (1)$$

in which σ_m is the Mott cross section, and A and B are given in terms of the deuteron charge (G_c), quadrupole (G_q) and magnetic (G_m) form factors:

$$\begin{aligned} A(Q^2) &= {G_c}^2 + (8\tau^2/9)\,{G_q}^2 + (2\tau/3)\,{G_m}^2 \\ B(Q^2) &= 4\tau(1+\tau)\,{G_m}^2/3 \end{aligned} \qquad (2)$$

with Q^2 the square of the 4-momentum transfer and $\tau = Q^2/4{m_d}^2$. Thus, a Rosenbluth separation may be used to extract A and B (and hence G_m) from scattering data, but G_c and G_q may not be separated. To isolate these form factors requires the use of polarization techniques. Following the Madison convention[1], the scattering of unpolarized electrons from a tensor polarized deuteron is described by the cross section[2]

$$\frac{d\sigma}{d\Omega} = \sigma_0 \Big[1 + T_{20}\, t_{20} + 2\, T_{21}\, \mathrm{Re}(t_{21}) + 2\, T_{22}\, \mathrm{Re}(t_{22}) \Big] \qquad (3)$$

in which the T_{2i} and t_{2i} are respectively the components of the analyzing power and polarization tensors, in a spherical basis. For moderate momentum transfers and suitably chosen polarization directions, the terms involving T_{21} and T_{22} are small, and may be ignored for the moment. The tensor analyzing power T_{20} is given by:

$$\begin{aligned} T_{20} &= -\sqrt{2}\Big[X(X+2) + Y/2 \Big] \Big/ \Big[2(X^2+1) + 1 \Big] \\ X &= \frac{2}{3}\tau \left(\frac{G_q}{G_c} \right) \\ Y &= \frac{1}{3}\tau \left(\frac{G_m}{G_c} \right)^2 \Big[1 + 2(1+\tau)\tan^2(\theta/2) \Big] \end{aligned} \qquad (4)$$

and the tensor polarization t_{20} is given by:

$$t_{20} = p_{zz}\, P_2(\hat{n}\cdot\hat{q})/\sqrt{2} \tag{5}$$

in which P_2 is the second Legendre polynomial, $\hat{n}$ is the polarization direction, $\hat{q}$ is the momentum transfer direction, and p_{zz}, the polarization in a cartesian basis, is given by $1-3n_0$, in which n_0 is the fraction of deuterons with zero spin projection.

The effect of T_{20} (and also T_{21} and T_{22}) on the cross section is manifested as an asymmetry observed when either the target polarization p_{zz}, the polarization direction $\hat{n}$, or the azimuthal scattering angle is changed. At moderate momentum transfers and scattering angles, the terms involving X are dominant. Thus, T_{20} becomes very sensitive to the predicted zero crossing of G_c at a Q^2 of ~ 0.6 GeV^2. This zero crossing depends sensitively on details of the deuteron wave function and meson exchange effects. Thus, a measurement of T_{20} can be combined with existing data on A and B to extract all three deuteron form factors, and determine the deuteron wave function. In addition, T_{20} is insensitive to nucleonic electromagnetic form factors, such as the poorly known G_{en} which cancels out of the expression for X. Thus, a measurement of T_{20} probes the deuteron's structure directly.

These ideas are illustrated in figures 1 and 2, in which are shown the world data on A and B, and the data for T_{20} published prior to this experiment, together with a representative sample of theoretical curves[3-7] . The curves represent "realistic" calculations involving different nucleon potentials, mesonic degrees of freedom, relativistic effects, and nucleon form factors. In addition, we show the perturbative QCD prediction

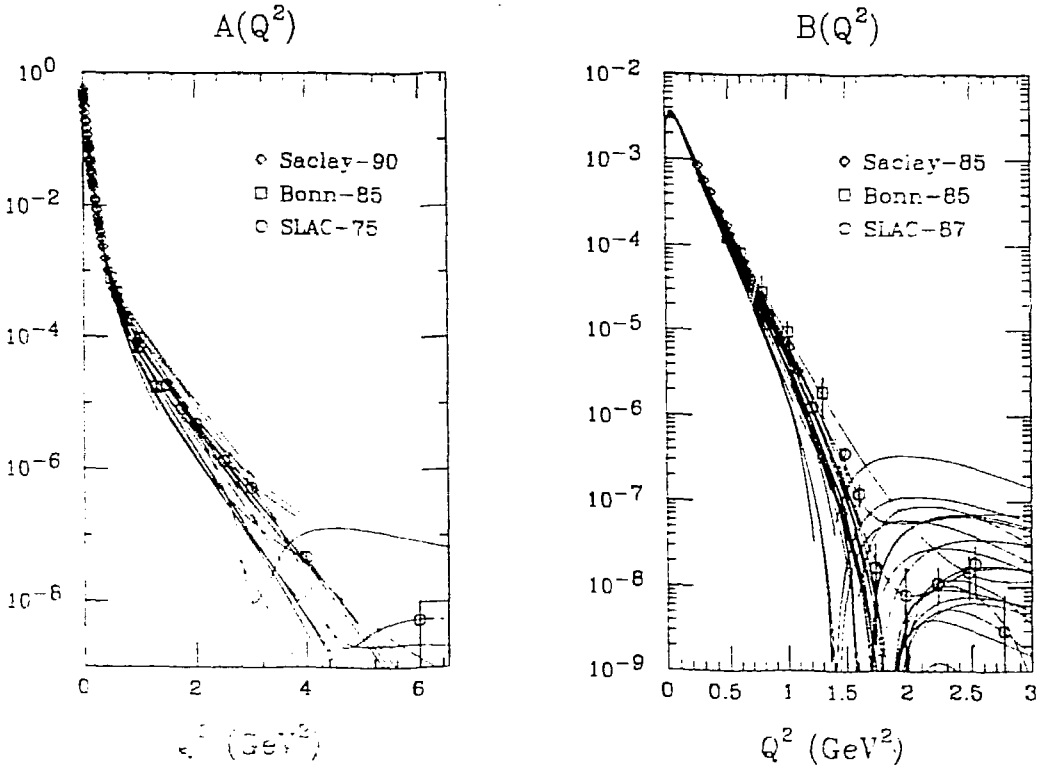

Fig. 1. World data and theoretical calculations for: (a) $A(Q^2)$, (b) $B(Q^2)$. The curves are from ref. 3-.

of Carlson, et al.[8] for T_{20}. The theoretical calculations will be discussed in more detail below. However, two points may now be observed: First, the curves for A and B spread over a large range of values. As we shall see later, there are relatively few calculations that simultaneously fit the data for A and B. Second, the data for T_{20} do not extend to a high enough Q^2 to distinguish between any of the theories. But above a Q^2 of ~ 0.6 GeV^2, the curves for T_{20} diverge quite widely, reflecting the sensitivity to G_c, and meson exchange currents.

Accurate data at these momentum transfers has been desired for many years in order to resolve the situation. We have undertaken a series of measurements at the VEPP-3 accelerator in Novosibirsk to measure T_{20} out to $Q^2 \sim 1$ GeV^2. The experiment has been divided into three phases, which will provide results at increasingly higher momentum transfers. The first phase of this experiment is now complete[9], with data for $Q^2 < 0.35$ GeV^2, the second phase is underway, and the third is expected to run in the next two years. In addition to the physics goals, this work is notable in that it represents the first use of polarized atoms in a storage tube as an internal target in an electron storage ring.

EXPERIMENT

This experiment was performed by the ANL/INP collaboration at the VEPP-3 electron storage ring at the Institute of Nuclear Physics in Novosibirsk, USSR. Electrons of 2.0 GeV were circulated around the ring at a frequency of 4 Mhz in a 1.0 ns bunch to form a current of up to 0.2 amps. In a straight section of the ring, the electrons passed

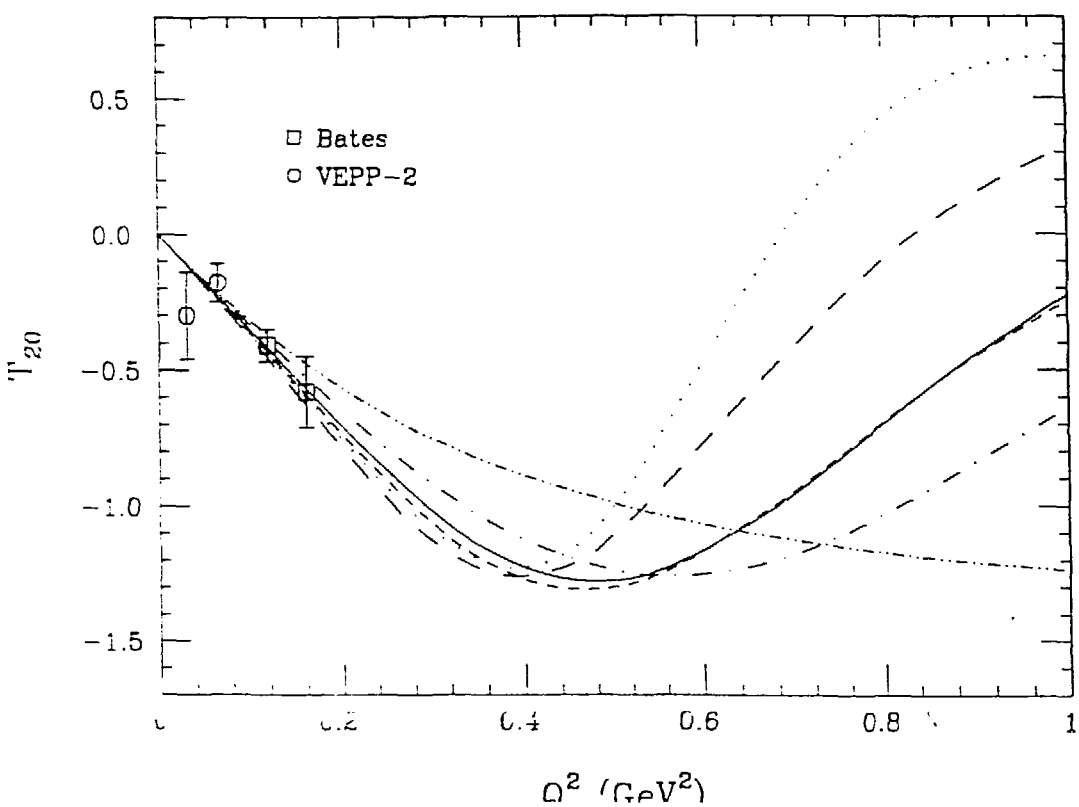

Fig. 2. World data (prior to this work) and theoretical calculations for T_{20}. The curves are from the same calculations as Fig. 1.

through a fixed, windowless, Al. storage tube, as shown in figure 3. The tube was 940 mm long, with an elliptical cross section of 24 mm × 46 mm, slightly larger than the cross section of the electron beam at injection. (The beam cools to a profile of 0.8 × 2.4 mm after injection.) Polarized deuterium atoms with $|p_{zz}| \sim 1$ from a conventional atomic beam source[10] were injected into the tube through an inlet pipe at the side. A small portion of this beam passed through an exit slit in the storage tube and continued to a polarization monitor, consisting of a Rabi magnet followed by a beam profile monitor. Most of the atoms entering the storage tube randomly bounced from wall to wall until exiting out either end of the tube. The mean storage time was 7.5 ms, during which an atom made 400 bounces, on average. To inhibit depolarization during collisions with the wall, the storage tube was coated with drifilm[11]. Based on measurements of target polarization, the depolarization probability per bounce was estimated to be less than 1×10^{-3}.

The atomic beam source produced a flux of 1×10^{16} atoms/s with polarization $|p_{zz}| = 1$. This tensor polarization was achieved by passing the beam through a sextupole magnet followed by an RF unit to induce transitions between the hyperfine states. The sign of p_{zz} could be chosen by inducing different sets of transitions within the RF section. 50% of the atoms in the beam were injected into the storage cell, forming a gas target of total thickness 3×10^{12} atoms/cm^2. This is 15 times thicker than was previously possible with the atomic beam-jet alone. However, only the central 6 cm were visible to the detectors, so that the useful target thickness was 6×10^{11} atoms/cm^2.

The average polarization of atoms in the cell, $\bar{p}_{zz}$, was determined to be $0.57 \pm .05$, as discussed below. This value is somewhat higher than the wall bounce depolarization

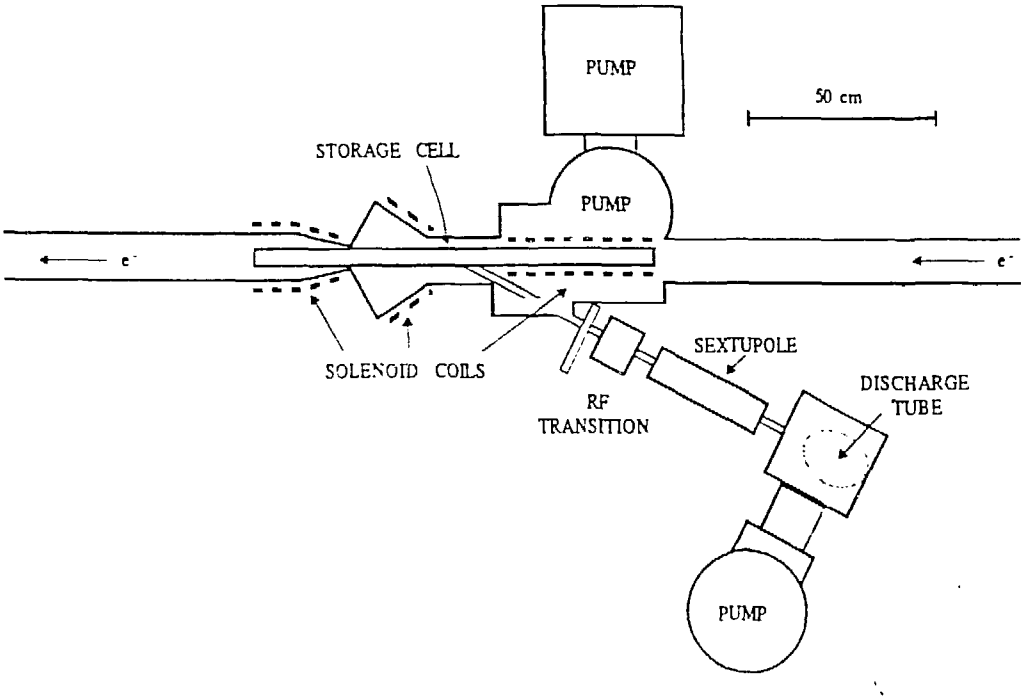

Fig. 3. Storage cell, scattering chamber, and atomic beam source. Not shown is the polarization monitoring equipment, the transverse field magnet surrounding the center of the cell, or the detectors for the scattered particles.

would predict. It is speculated that the longitudinal holding field of ~ 300 gauss created by solenoidal coils wound around the cell suppressed the wall bounce depolarization even further. The average polarization was monitored throughout the experiment, and was stable throughout the 6 months of running, during which 1 MC of electrons passed through the cell. This clearly shows that drifilm coated storage cells can survive the harsh radiation environment of an electron ring.

Scattered particles left the storage cell through 80 μm windows etched in the sides, passed through 100 μm Ti vacuum windows, and entered four nearly identical detector systems[12], as shown in figure 4. Each system consisted of separate arms to detect the scattered electrons and deuterons. Both arms consisted of six planes of drift chambers to determine the particle trajectory, followed by scintillation counters to identify the particle. In the electron arm, the counter was a 1 cm thick plastic scintillator, viewed by a phototube, and preceded by a 5 radiation length thick Pb plate. The deuteron counters were composed of three layers of plastic scintillator of thickness 0.5, 1.0, and 1.0 cm, followed by a segmented counter of either 20 cm of plastic scintillator, or 16 cm of NaI, all viewed by phototubes. The detectors accepted electrons scattered between 10° and 22°, in a 40° range of φ, and deuterons in the corresponding range $68° \leq \theta_d \leq 80°$.

In the portion of the cell visible to the detectors, the polarization direction of the deuterons was aligned in a transverse direction ($\vec{n}_1$ or $\vec{n}_2$) by applying a transverse magnetic field of 700 gauss. Thus, for a given system, the polarization direction and momentum transfer direction are nearly parallel or nearly perpendicular, so that the t_{20} term of eq. (3) induces an azimuthal asymmetry in the scattering rates of the four systems. This asymmetry may be rotated by 90 degrees by switching the magnetic

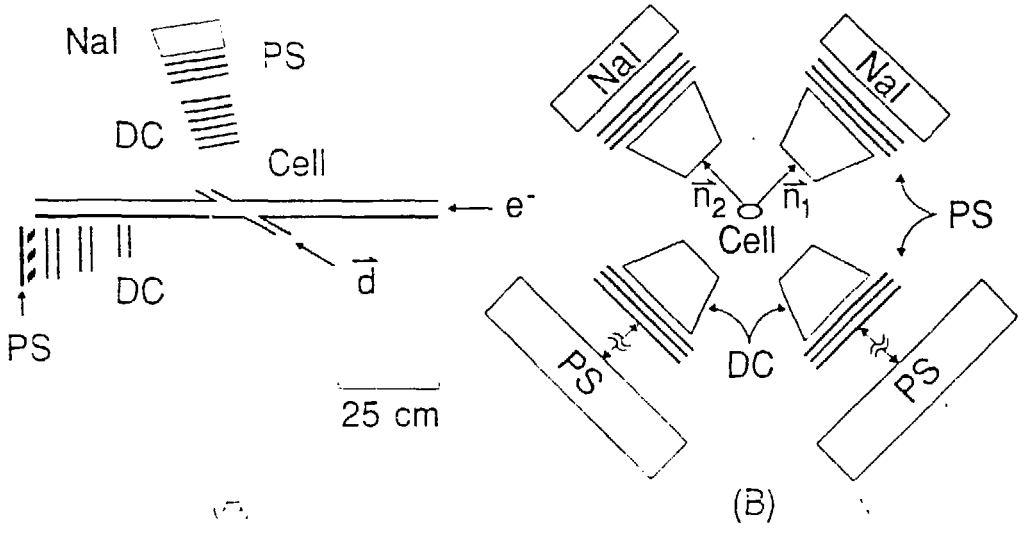

Fig. 4. Storage cell and detector systems. (A) Side view. Only one detector system is shown. (B) Axial view. Only the deuteron arms are shown. Not shown: central magnet to provide transverse field along $\vec{n}_1$ or $\vec{n}_2$.

field between $\vec{n}_1$ and $\vec{n}_2$, or reversed by changing the sign of p_{zz}. With four systems, two signs of p_{zz}, and two polarization directions, there are 16 scattering rates that may be observed. By combining all 16 rates into a global asymmetry, a large reduction in systematic uncertainties is achieved. Systematic uncertainties were further reduced by reversing the sign of p_{zz} every two minutes during the 1-2 hr runs following beam injection into the ring, and by switching the magnetic field between each run.

DATA ANALYSIS

The trigger for this experiment consisted of a coincidence between the scintillators in the electron and deuteron arms, as well as a minimum number of hits in the drift chambers. (A tagged photon trigger also existed to study photodisintegration events, but this work will not be considered here.) This trigger effectively suppressed background due to stray beam particles, but did not distinguish between elastic electron-deuteron scattering and $(e, e'p)$ events. In fact, the elastic events comprised less than 3% of the data, so that a principal task of the data analysis was to separate deuterons from the much larger proton background.

This separation relied on kinematical correlations between the scattered electron and deuteron, and on the differences in specific ionization between the proton and deuteron. An example of this is shown in figure 5. In Fig. 5a, we see a plot of the electron scattering angle vs. the amplitude (corrected for position variations) of the first thin scintillation counter (A_1). The events cluster into two bands due to deuterons and protons. In Fig. 5b we plot the amplitudes of the second vs. first thin counter, for events that penetrate further than the first counter. Particles of the lowest energy deposit negligible energy in the second counter, and a maximum in the first. Particles of higher energy deposit less energy in the first layer and more in the second, so that the events cluster into bands. The deuteron and proton bands are distinct because of their different specific ionizations. Particles reaching the third counter of the thick counter

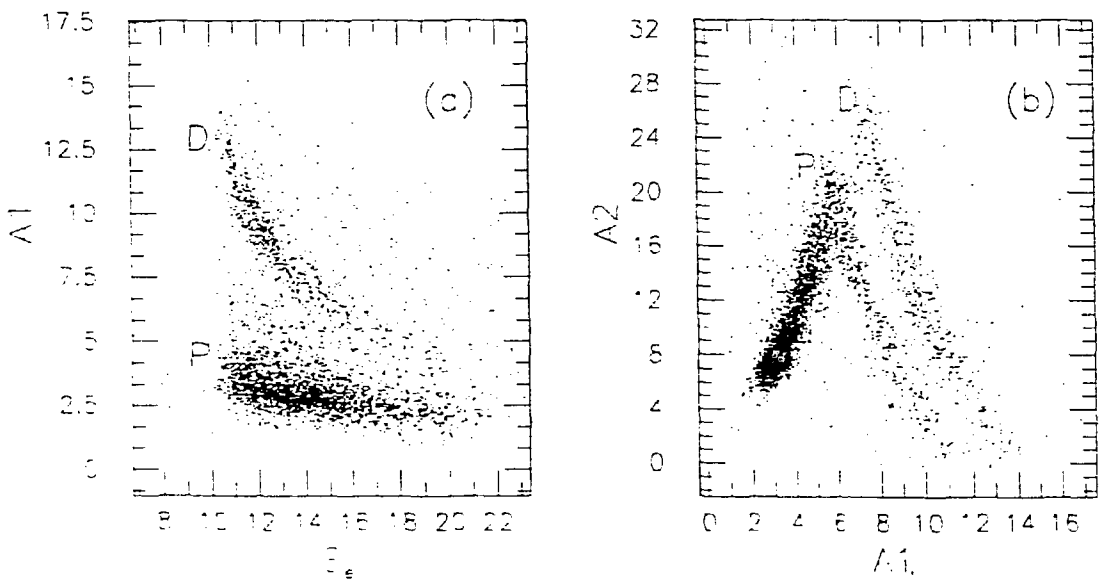

Fig. 5. Event distributions used in particle identification. (A) Correlation between electron scattering angle and amplitude from the first thin counter. (B) Correlation between amplitudes from the first and second thin counters.

are not resolved here, but a similar technique may be used with the amplitudes from the last two counters penetrated by the particle.

Figure 6 shows the correlation between electron and deuteron scattering angles. The sum of the electron and deuteron scattering angles is plotted in Fig. 6a and the difference in phi angles is plotted in Fig. 6b, after all other cuts have been applied. The elastic events cluster in a large peak, with a small background of remaining proton events. After a final cut on these correlations, the background is sufficiently suppressed that it may be ignored.

The remaining elastic events were then grouped into three momentum transfer bins, based on which counter the particle stopped: A_2, A_3, or the thick counter, and further grouped according to the magnetic field direction and sign of p_{zz}. The number of events in each bin was normalized by the collected charge, and the resulting scattering yields were reduced to an experimental asymmetry defined as:

$$a_{\rm exp} = \left[(S^2_{1+} - S^2_{1-} - S^2_{2+} + S^2_{2-}) - (S^1_{1+} - S^1_{1-} - S^1_{2+} + S^1_{2-})\right] / \sum S^i_{jk} \qquad (6)$$

in which S^i_{jk} is the sum of the counting rates in the detector systems facing the directions $\pm n_i$, with the magnetic guide field pointing in direction n_j, and the sign of p_{zz} given by k. The values of $a_{\rm exp}$ so obtained are listed in table 1.

To extract T_{20} from these asymmetries it is necessary to know the average target polarization $\bar{p}_{zz}$. This quantity was not measured directly, but instead was determined

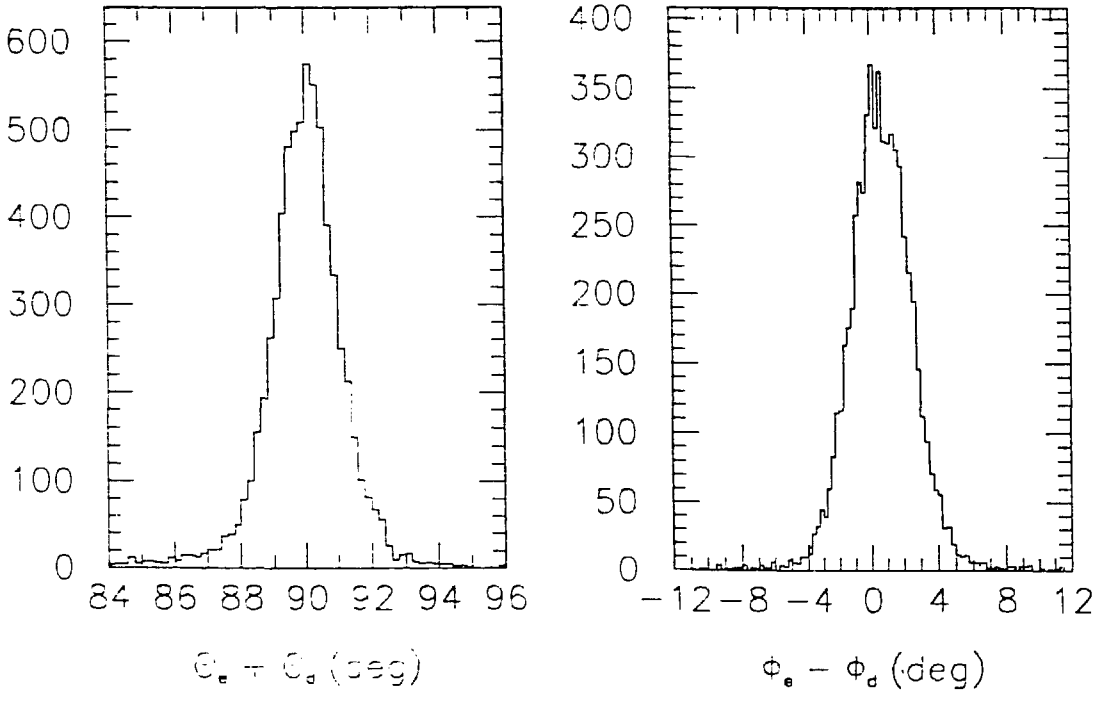

Fig. 6. Correlation between the electron and deuteron scattering angles, after application of all other cuts. (A) The sum of θ_e and θ_d. (B) The difference $\varphi_e - \varphi_d$.

Table 1. Experimental results. The results at the lowest Q for a'_{exp} and T_{20} are normalized to predictions from the Paris potential.

$\bar{Q}^2$ (GeV^2)	a_{exp}	a'_{exp}	T_{20}
0.150	$0.140 \pm .013$	0.245	-0.538
0.242	$0.189 \pm .038$	$0.330 \pm .073$	$-0.77 \pm .16 \pm .07$
0.335	$0.309 \pm .077$	$0.539 \pm .14$	$-1.32 \pm .32 \pm .11$

by normalizing a_{exp} at the lowest Q^2 to the prediction of theory. For this purpose, we used a PWIA calculation based on the non-relativistic wavefunctions of the Paris potential, including such effects as detector acceptances and non-zero values for t_{21} and t_{22}. At this momentum transfer, the theoretical ambiguity is small, with a systematic uncertainty of $< 5\%$. We thus determined $\bar{p}_{zz} = 0.57 \pm .05$. This was used to compute $a'_{exp} = a_{exp}/\bar{p}_{zz}$, the asymmetry we would have observed in the case of perfect target polarization. T_{20} is then given by:

$$T_{20} = a'_{exp}/\bar{t}_{20} + [\text{corrections for } T_{21},\, T_{22} \text{ terms}] \qquad (7)$$

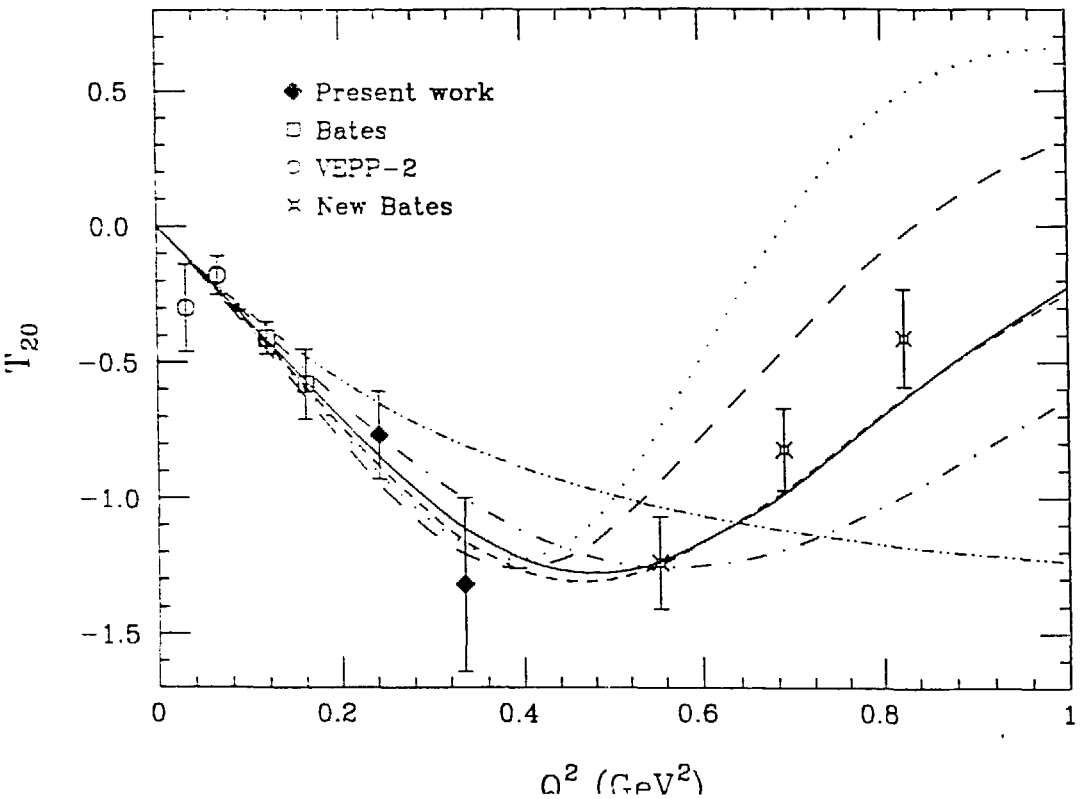

Fig. 7. Experimental results and theoretical predictions for T_{20} as a function of the momentum transfer. The error bars represent statistical and systematic uncertainties added in quadrature. The solid, short-dashed, and dot-dashed lines are from [7], and represent the Paris, V_{14}, and Bonn Q potentials. The dotted and dashed lines are from models C' and D' of [4].

The effective tensor polarization components, $\bar{t}_{20}$, $\bar{t}_{21}$, and $\bar{t}_{22}$ were obtained by averaging the values for a fully polarized deuteron over the acceptance of the apparatus. The latter two were combined with predictions for T_{21} and T_{22} from the non-relativistic Paris potential to compute the correction terms in eq. 7. These respectively amount to +10% and - 1.7% of the total asymmetry for $\bar{Q} = 2.93$ fm^{-1}, the worst case. The resulting values for T_{20} are also listed in table 1, and plotted in figure 7. Also shown are the results at lower Q from previous experiments at Novosibirsk[13] and Bates[14], and the results at higher Q from the Bates/Ahead collaboration[15], discussed elsewhere in these proceedings.

Several theoretical predictions for T_{20}, based on realistic nucleon potentials, as well as a prediction based on perturbative QCD, overlay the data in figure 7. Above a Q^2 of 0.35 GeV^2, the potential-based curves are strongly divergent, largely due to differences in G_c. The PQCD result is even more divergent, falling towards an asymptotic value of $-\sqrt{2}$ for large Q^2. The data from our experiment do not extend to a high enough Q^2 to distinguish between the curves, whereas the new data from Bates clearly rule out the PQCD curve and are also inconsistent with the C' and D' models of Blunden et al. and the Bonn-Q result of Chung et al. Our results are currently limited to $Q^2 < .35$ GeV^2 by the luminosity available at VEPP-3 with this target. However, improvements are underway to use a higher density storage cell, new detectors, and an optically pumped source of polarized deuterons to increase the luminosity by a factor of ~ 50. This will allow us to measure T_{20} for $Q^2 \sim 1$ GeV^2 with smaller error bars than the present data from Bates.

COMPARISON OF THEORY WITH DATA

With data for T_{20} now extending to 0.82 GeV^2, it is quite interesting to simultaneously compare theoretical predictions with data for all three form factors. At issue are such questions as the form of the nucleon potential, the importance of relativistic effects and meson exchange currents, and the poorly known nucleon form factors, in particular G_{en}. We shall consider five representative sets of models which address these effects: The work of Blunden et al.[4], Dymarz et al.[5], Schiavilla-Riska[3], Chung et al.[7], and Hummel-Tjon[6].

The first three are non-relativistic calculations. Blunden et al. present a coupled channel model (NN, NΔ, $\Delta\Delta$, NN*) explicitly including isoscalar meson exchange currents. We consider the C' and D' models with Hoehler (H) and Gari-Krumpelmann (GK) form factors. Dymarz et al. also use the coupled channel formalism in which virtual Δ isobars are explicitly included. The work is based on a OBE model, also including MEC. Schiavilla and Riska use the Argonne v_{14} potential to construct an exchange-current consistent with current conservation, with MEC explicitly included.

The latter two calculations are based on a relativistic framework. Hummel and Tjon use covariant wavefunctions based on the one-boson-exchange model, using either H or GK form factors, with MEC explicitly included. Chung et al. use Hamiltonian light-front dynamics to derive wavefunctions based on non-relativistic NN potentials. No explicit isoscalar MEC are included. They investigated a variety of commonly used NN potentials, with both H and GK form factors.

The comparison of the predictions for A, B, and T_{20} with the data is presented in table 2. Each calculation was judged by eye to be either in good agreement (+), clear disagreement (-), or questionable agreement (?). Although subjective, this ranking illustrates several points. First, no model is able to obtain an excellent fit (all pluses) to all the data. Second, only two models have no clear disagreement with the data (no minuses). Interestingly, these are two relativistic models which use Gari-Krumpelmann form factors, although in other details they are quite different. And lastly, neither of the coupled channel calculations is able to simultaneously fit A and B.

Table 2. Comparision of theoretical models with experiment. The quality of agreement between models and data for T_{20}, A, and B was judged by eye. A '+' signifies good agreement, a '-' signifies clear disagreement, and a '?' signifies questionable agreement. A and B are judged separately for Q^2 below and above 1.5 Gev^2. Models without clear disagreement are flagged by a star at the left.

		A		B		T_{20}
	Theory	Hi Q^2	Low Q^2	Hi Q^2	Low Q^2	
	Schiavilla-Riska	+	+	+	+	-
	Blunden et al.					
	C' (H)	?	?	-	?	-
	C' (GK)	-	-	+	+	-
	D' (H)	+	?	-	-	-
	D' (GK)	-	+	+	?	-
	Dymarz et al. (W1)					
	NN	?	+	-	-	?
	NN+$\Delta\Delta$	?	+	-	-	?
	NN+$\Delta\Delta+\pi\pi$	-	-	+	+	?
	NN+$\Delta\Delta+\pi\pi+\pi\rho\gamma$	?	-	-	-	+
	Hummel-Tjon					
	IA (H)	-	-	-	-	+
	$\pi\rho\gamma$ (H)	?	-	-	-	+
	$\pi\rho\gamma+\omega\epsilon\gamma$ (H)	-	-	+	?	?
*	$\pi\rho\gamma+\omega\epsilon\gamma$ (GK)	+	+	+	?	?
	Chung et al.					
	Paris (H)	-	+	?	-	?
	Paris (GK)	+	?	?	-	?
	AV14 (H)	-	+	+	?	?
*	AV14 (GK)	+	?	+	?	?
	Bonn-E (H)	-	-	?	-	-
	Bonn-E (GK)	-	?	+	?	-
	RSC (GK)	+	?	-	-	+

SEPARATION INTO G_c AND G_q.

With data in hand for A, B, and T_{20}, it is possible to extract values for G_c and G_q with which to compare these models. The world data for A and B was fit with smooth functions to remove statistical fluctuations, and the resulting values were combined with the T_{20} data to extract $|G_c|$, $|G_q|$, and $G_c \cdot G_q$. These values are plotted in figure 8. The error bars are given by:

$$\Delta G^2 = (\partial G/\partial T_{20})^2 \, \Delta {T_{20}}^2 + (\partial G/\partial A)^2 \, \Delta A^2 + (\partial G/\partial B)^2 \, \Delta B^2 \qquad (8)$$

except for the points at $Q^2 = 0.34$ GeV^2 and 0.55 GeV^2, where we have simply plotted the solution corresponding to one of the endpoints of the T_{20} error bar. (The other endpoint lies in a physically unallowed region, as does the data point at $Q^2 = 0.55$ GeV^2.)

From a change in the sign of $G_c \cdot G_q$, we infer a change in the sign of G_c for the highest Q^2 of the new Bates data, indicating a zero-crossing of G_c. The three curves in figure 8 correspond to the three models which can simultaneously fit A and B. Interestingly, the G_c predictions of Chung et al. and Hummel-Tjon lie almost directly on top of each other! They also predict a zero-crossing that agrees well with the data. On the

other hand, the curve for Schiavilla-Riska places the zero-crossing at too low a momentum transfer. Schiavilla-Riska has an excellent fit to A and B, but the misplacement of the G_c zero-crossing evidently disturbs the agreement with T_{20}. In general, we find that models with a G_c zero-crossing at too low a value of Q^2 result in T_{20} predictions that lie above the new data, and models with a zero-crossing at too high a value of Q^2 lie below the T_{20} data. Thus, the T_{20} data strongly constrains the location of this zero.

CONCLUSIONS

In conclusion, we have measured the asymmetry in electron-deuteron elastic scattering to determine T_{20} for momentum transfers $Q^2 < .34$ GeV^2. This work represents the first use of a polarized atoms in a storage tube as an internal target in an electron storage ring. Work is in progress to extend these measurements to $Q^2 \sim 1$ GeV^2 through the use of a high density target cell and a high-flux, optically pumped source of polarized deuterons. Although the present results cannot distinguish between theoretical models, they may be combined with recent results from Bates to show a clear minimum in T_{20} for $Q^2 \sim 0.45$ GeV^2, in contrast to the PQCD predictions of ref. 8. A comparison between these data and the predictions of several theoretical models shows that it is difficult to simultaneously fit the data for A, B, and T_{20}. Separation of the data into G_c and G_q reveals that G_c passes through zero near $Q^2 = 0.75$ GeV^2. The theoretical predictions for T_{20} are very sensitive to the placement of this zero, and some models are

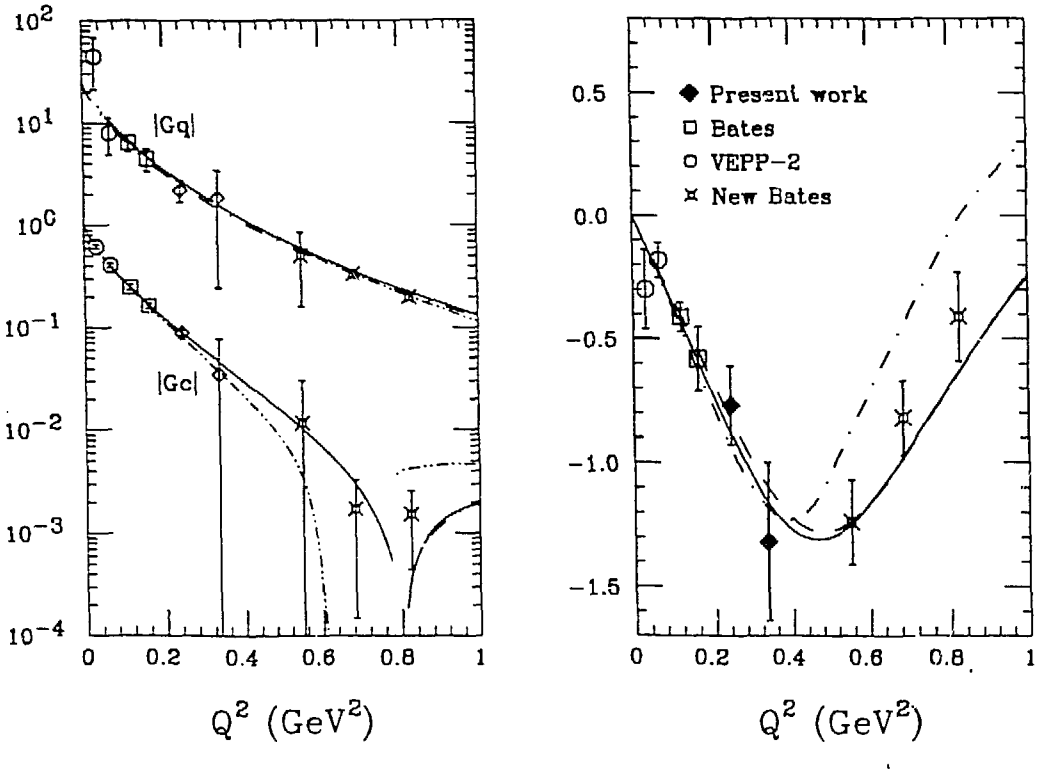

Fig. 8. Values for G_c and G_q extracted from the data for A, B, and T_{20} are plotted in (a). T_{20} is plotted in (b). The solid curve is the prediction of Chung et al. (Argonne v_{14}, GK), the dashed curve is the prediction of Hummel-Tjon ($\pi\rho\gamma + \omega\epsilon\gamma$, GK), and the dotted curve is the prediction of Schiavilla-Riska.

in clear disagreement with the new results. However, the situation remains ambiguous, and further experimental and theoretical results are eagerly awaited.

ACKNOWLEGEMENTS

I would like to acknowlege the efforts of the INP and ANL collaboration members and staff in performing the T_{20} measurements at VEPP-3. This work was supported by the U.S. Department of Energy, Nuclear Physics Division, under contract No. W-31-109-ENG-38, the Soviet Academy of Science, and the Soviet-American Committee for the Investigation of Fundamental Properties of Matter.

REFERENCES

1. *Proceedings of the Third International Symposium on Polarization Phenomena in Nuclear Reactions, Madison, Wisconsin, 1970,* edited by H. H. Barschall and W. Haeberli, p. xxv.
2. T. W. Donnelly and A. S. Raskin, Ann. Phys. (N.Y.) **169**, 247 (1986); V. F. Dmitriev, S. G. Popov and, D. K. Toporkov, Institute of Nuclear Physics, Novosibirsk, Report No. 76-85, 1976 (unpublished).
3. R. Schiavilla and D. O. Riska, Phys. Rev. C **43**, 437 (1991).
4. P. G. Blunden, *et al.*, Phys. Rev. C **40**, 1541 (1989).
5. R. Dymarz and F. C. Khanna, Nucl. Phys. **A507**, 560 (1990).
6. E. Hummel and J. A. Tjon, Phys. Rev. Lett. **63**, 1788 (1989).
7. P. L. Chung itet al., Phys. Rev. C **37**, 2000 (1988).
8. C. Carlson, Nucl. Phys. **A508**, 481c (1990).
9. R. Gilman *et al.*, Phys. Rev. Lett. **65**, 1733 (1991).
10. A. V. Evstigneev, S. G. Popov and D. K. Toporkov, Nucl. Instrum. Methods Phys. Res., Sect. **A 238**, 12 (1985).
11. L. Young *et al.*, Nucl. Instrum. Methods Phys. Res., Sect. **B 24/25**, 963 (1987); D. R. Swenson and L. W. Anderson, Nucl. Instrum. Methods Phys. Res., Sect. **29**, 627 (1988).
12. B. B. Wojtsekhowski *et al.*, Institute of Nuclear Physics, Novosibirsk, Report No. 88-120 (to be published).
13. V. F. Dmitriev *et al.*, Phys. Lett. **157B**,143 (1985); B. B. Wojtsekhowski *et al.*, Pis'ma Zh. Eksp. Teor. Fiz. **43**, 567 (1986) [JETP Lett. **43**, 733 (1986)].
14. M. E. Schulze *et al.*, Phys. Rev. Lett. **52**, 597 (1984).
15. I. The, *et al.*, Phys. Rev. Lett. **67** 173 (1991).